The influence of longwave cloud-top cooling on marine stratocumulus cloud transitions

By
© 2017
Prescott Bishop
B.Sc. Meteorology, Texas A&M University, 2010

Submitted to the graduate degree program in Atmospheric Science and the Graduate Faculty of the University of Kansas in partial fulfillment of the requirements for the degree of Master of Science.

Chair: Dr. David Mechem

Dr. Nathaniel Brunsell

Dr. David Rahn

Date Defended: 21 April 2017

The thesis committee for Prescott Bishop certifies that this is the approved version of the following thesis:

The influence of longwave cloud-top cooling on marine stratocumulus cloud transitions

Chair: Dr. David Mechem

Date Approved: 21 April 2017

Abstract

The nocturnal transition (beginning around sunset) of the turbulent structure within the stratocumulus-topped boundary layer in the Southeast Pacific is simulated using near-LES model framework and sounding data from the Variability of American Monsoon Systems (VAMOS) Ocean–Cloud–Atmosphere–Land Study Regional Experiment (VOCALS-REx) as the initial conditions. In addition to the control simulation, 4 sensitivity analyses are conducted by varying the longwave radiative flux (ΔF_n) across the boundary layer, thereby varying the maximum permitted radiative cooling. These radiative cooling values are constrained through a radiative-transfer calculation using all the VOCALS sounding data and liquid water path retrievals. The magnitude of radiative cooling is shown to impact boundary layer properties such as stability, cloud-top height, cloud-cover, and precipitation. For all simulations, the top-down mechanism of radiative cooling dominates over the first few hours, as downdrafts penetrate lower and lower and destabilize the boundary layer to deep-layer circulations, which in these simulations are largely surface-based cumulus-like updrafts. The simulations with stronger ΔF_n undergo this transition sooner and exhibit higher cloud-top heights, stronger overall turbulence, increased precipitation, and a better-sustained cloud cover. Increases in precipitation with stronger radiative forcing arise largely through increases in precipitation area rather than intensity of drizzle cells. Simulation behavior of the transition is found to be broadly consistent with the VOCALS sounding composites and exhibits similar self-limiting drizzle behavior found in the observations.

Acknowledgments

We want to thank Marat Khairoutdinov for providing SAM to the atmospheric science community. Paquita Zuidema for the liquid water path retrieval data. Thanks to Qiang Fu for the use of his radiation code. U.S. National Oceanic and Atmospheric Administration (NOAA) Climate Program Office (CPO) Climate Prediction Program for the Americas (CPPA) Grants GC09-252b, GC09-507, and NA10OAR4310160….

Table of Contents

Chapter 1. Introduction

Stratocumulus are Earth's most abundant cloud type, commonly exceeding a million square kilometers in area and, on average, covering a fifth of the planet's surface (Nicholls et al. 1984). Warren et al. (1986) noted that stratocumulus coverage includes roughly 23% of the ocean and 12% of land. Stratocumulus clouds generally form within the planetary boundary layer (PBL), in regions of strong subsidence capped by a strong inversion layer (Wood 2012). Schubert et al. (1979) observed that these cloud decks most commonly persist in the subtropical and mid-latitude regions along the western coasts of the major continents under conditions of large-scale subsidence associated with the downward branches of both the Hadley and Walker circulations.

The stratocumulus-topped boundary layer (STBL) significantly impacts the amount of incoming shortwave radiation that the ocean absorbs (Stephens and Greenwald 1991). The profound influence of stratocumulus is due both to the extensive area that these clouds cover and their high contrast in albedo with the dark ocean surface below. The temperature of the stratocumulus cloud top is relatively close to the temperature of the ocean surface, resulting in a similar upwelling longwave flux whether clouds are present or not. By more significantly impacting the Earth's incoming shortwave radiation than outgoing longwave radiation, stratocumulus lead to a net cooling of ~100 W m^{-2} (Hartmann and Short 1980). Slingo et al. (1990) theorized that a mere 15-20% increase in the areal coverage of marine stratocumulus can completely offset the heating caused by doubling the amount of greenhouse gases. The potential impacts of climate change on the areal coverage of stratocumulus are not well understood, which contributes to the large

uncertainty in the cloud–climate feedbacks (Bony and Defrense 2005, Medeiros et al. 2008, Medeiros and Stevens 2011, Stevens and Bony 2013).

Over 30 years ago, Nicholls et al. (1984) recognized that understanding the dynamical processes affecting the coverage of these cloud systems in our current climate is crucial to improving global climate models making projections of future climate. Small changes in location or synoptic meteorological conditions such as subsidence or advection can have a strong influence on the variability of turbulence, precipitation, and cloud cover within the STBL. Lilly et al. (1968) theorized that much of this variability results from differences in the strength of cloud-top radiative cooling, which is the primary source of turbulence within the boundary layer. Nicholls et al. (1986) found a thin (~10 m) layer between the top of the stratocumulus deck and the base of the inversion known as the entrainment interface layer (EIL). In this layer, water vapor significantly decreases with height while the potential temperature experiences a sharp increase. Deardorff et al. (1980a) explained that variations in stability in this layer arise during the nighttime hours, when radiative cooling along the cloud-top leads to density fluctuations in the EIL that generate turbulent, entraining downdrafts which may be enhanced by evaporative cooling within the cloud layer. These entraining downdrafts are consistent with a negative skewness in the vertical motion field that develops in the cloud layer as shown in Young et al. (2000). The entraining effects of the radiative cooling however, are mainly restricted to the nighttime hours, and Park et al. (2005) found that shortwave heating of the cloud layer makes the generation of turbulence via cloud-top longwave radiative cooling much less effective.

These radiatively driven downdrafts can change the character of turbulence-generating mechanisms in the STBL. Albrecht et al. (1995) explains that a conditionally unstable layer formed by the entrainment-driven circulations warms the cloud layer, decoupling it from the subcloud layer. According to Krueger et al. (1995), this decoupling cuts off the moisture supply of the ocean surface from the cloud layer, resulting in thinning of the stratiform clouds that were previously sustained by deep-layer mixing. This behavior is largely consistent with the Wyant et al. (1997) conceptual model of boundary-layer decoupling accompanying steadily warming sea-surface temperatures (SSTs). With the bulk of the moisture now contained within the subcloud layer, conditional instability builds in the lower STBL leading to surface-driven updrafts taking the form of cumulus clouds rising into the thinning stratiform deck.

Drizzle from stratocumulus can also enhance this transition to surface-driven cumuliform circulations. Stevens et al. (1998) found that precipitation produces a net latent heating in the cloud layer and evaporative cooling in the subcloud layer, which both tend to stabilize the boundary layer. Furthermore, vanZanten and Stevens (2005) observed that drizzling stratocumulus often leads to the formation of cold pools, which are often found in pockets of open cells (POCs, Stevens et al. 2005a). In numerical simulations, new cells preferentially form at the cold pool boundaries (Wang and Feingold 2009a, b), just as for deep convection, and hence the cold pools tend to promote (or at the very least, be associated with) mesoscale organization.

Previous research outlined in this introduction has demonstrated that two main turbulence-generating mechanisms may be active in the STBL: cloud-top radiative cooling (“top-down”) and a surface-based cumulus dynamics (“bottom-up”). The

predominant forcing mechanism in unbroken stratocumulus is cloud-top cooling (top-down), whereas surface fluxes predominantly drive the turbulence associated with cumulus updrafts (bottom-up). One might also envision some form of transition between these two regimes, which simultaneously contains both top-down and bottom-up forcing mechanisms. However, the relative roles of the two mechanisms in establishing boundary-layer properties and mesoscale organization are not well understood. Focusing on the (VAMOS) Ocean–Cloud–Atmosphere–Land Study — Regional Experiment (VOCALS-REx, usually referred to as just "VOCALS"), Bretherton et al. (2010) found substantial variability in cloud cover, drizzle, stability, and radiative cooling rate in the Southeastern Pacific (SEP) stratocumulus, suggesting that the SEP is an ideal setting to evaluate the importance of these two turbulence-generating mechanisms. VOCALS ship observations exhibit substantial diurnal variability in cloud and precipitation properties, and diurnal transitions in Doppler-velocity variance and skewness, which implies distinct transitions in the character of the turbulence-generating mechanisms (Burleyson et al. 2013, 2015).

This research aims to investigate how differences in nocturnal longwave radiative forcing impact subsequent cloud, precipitation, and turbulence properties (both top-down and bottom-up) over the SEP. The observational component of the research quantifies the variability of cloud-top cooling over the SEP region using sounding observations from the NOAA R/V Ronald Brown (RHB) vessel during the entire VOCALS–REx field campaign in 2008. Meanwhile, the modeling portion of the study employs large-eddy simulation (LES) to evaluate in a controlled manner the sensitivity of the STBL cloud

properties, specifically cloud cover, precipitation, and turbulence, to differences in cloud top longwave cooling.

Chapter 2. Methodology

2.1 Description of control simulation

All simulations are based on the "Deep" case in Mechem et al. (2012) and employ the same "near–LES" approach using grid spacings considered relatively course (150 m horizontal grid spacing) compared to true large-eddy simulation. The near-LES approach resolves the bulk of turbulent transports while also permitting a sufficiently large domain to represent mesoscale variability that develops in drizzling stratocumulus (Savic-Jovcic and Stevens 2008). Initial conditions for the model are taken from Mechem et al. (2012) and are based on a sounding launched from the RHB on October 26, 2008 at 1127 UTC (0527 LT), near 19.6°S, 85.8°W. Potential temperature and moisture profiles are illustrated by Fig. 1, taken from Mechem et al. (2012), who extensively discusses the control simulation. These idealized simulations are run under perpetual nocturnal conditions.

The results of Burleyson (2013) show that turbulence decreases quickly after sunrise and that the boundary layer becomes stratified (stabilized, relative to a well-mixed boundary layer) almost immediately. The stratification peaks in the late afternoon, but soon begins to decrease as the solar heating diminishes, and the boundary layer ultimately re-couples nocturnally. The modeling portion of this study is particularly interested in how the boundary layer transitions from this stratified late afternoon

structure to the coupled nocturnal condition. Therefore the model initialization at dusk assumes that the boundary layer is initially stratified, with the sounding used indicative of a stable, decoupled boundary layer characteristic of late-afternoon conditions (Burleyson et al. 2013). Beginning with a stratified boundary layer, we can simulate the transition from top-down to bottom-up turbulence-generation mechanisms in response to varying radiative cooling magnitudes. Our simulations represent the transition that the decoupled, late-afternoon boundary layer structure experiences after the stabilizing influence of solar radiation is removed.

The model is run for 12 hours using 2-second time steps with the horizontal domain spanning 57.6×57.6 km^2 and a horizontal grid spacing (Δx and Δy) of 150 m. As in Mechem et al. (2012), the vertical grid has a total of 96 grid points and the grid spacing (Δz) is stretched unevenly as follows: 25 m at z=0; 40 m at z=800 m; 25 m at z=1800 m. The functional form of the vertical grid structure follows that of Ackerman et al. (2009). This configuration locates the smallest grid volumes at the surface and across the inversion where entrainment of free-tropospheric air takes place.

Surface fluxes are calculated from bulk aerodynamic theory, assuming a fixed SST of 291.4 K, which results in sensible and latent heating of approximately 5 and 55 W m^{-2}, respectively. The cloud and precipitation scheme uses the Kogan et al. (1991) method of size-resolved ("bin" or "explicit") microphysics with 34 droplet bins and 19 cloud condensation nuclei (CCN) bins. As in Mechem et al. (2012), all simulations assume an initial CCN concentration of 135 cm^{-3}, assuming a shape based on the distribution from the Rain In Cumulus over the Ocean (RICO) experiment (Snodgrass et al. 2008). The simulated radar reflectivity factor used to represent precipitation intensity

is calculated directly from the model drop size distribution (DSD) assuming the droplets act as perfect Rayleigh scatterers (~D^6), as in Mechem et al. (2012, 2015). Simulations include a spin-up period over the first 2 hours of the simulation in which a simple condensation adjustment is employed before the bin-microphysics condensation calculation is begun. Collision-coalescence is switched on after the second hour. This spin-up period is shorter than that used in Mechem et al (2012) but produces essentially similar results.

2.2. Configuration of sensitivity experiments to vary longwave flux

All simulations use the simplified radiation parameterization of Stevens et al. (2005b), where the net longwave radiation flux is calculated from the vertical profile of the liquid-water mixing ratio:

$$F_{rad}(x, y, z, t) = F_0 e^{-Q(z,\infty)} + F_1 e^{-Q(0,z)} \quad (1)$$

where $Q(a, b) = \kappa \int_a^b \rho r_l dz$. Here Q is the liquid water path, r_l is the liquid-water mixing ratio, ρ is the air density, and κ is a fixed tuning parameter. The parameters F_0 and F_1 represent the maximum in net longwave flux across cloud top and cloud base, respectively (Fig. 2). The net longwave radiation flux, F_{rad}, is the sum of the heat fluxes associated with cloud-top cooling (F_0) and cloud-base warming (F_1). As in Mechem et al., (2012), we project fluxes at cloud base and cloud top onto a single, redefined value of F_0, which then represents the net flux across the depth of the boundary layer:

$$F_{rad}(x, y, z, t) = F_0 e^{-Q(z,\infty)} \quad (2)$$

This method is computationally inexpensive and allows the specification the overall flux jump by varying F_0.

The parameter F_0 in the control simulation is calculated as in Mechem et al. (2012) by applying the δ–four-stream radiative transfer calculation of Fu and Liou (1992, 1993) to the observed sounding. The LWC profile was assumed to vary adiabatically with a maximum value of 0.5 g m^{-3} at 1.65 km above sea level, the height of the inversion. The choice of maximum LWC is rather arbitrary but above some minimum has a minor effect on the net radiative flux across the boundary layer. Figure 2 shows the net longwave flux profile for the control-simulation sounding, with F_0 equal to 105 W m^{-2} and F_1 equal to 25 W m^{-2}. Using the projection method, we set F_0 in (2) to be 105 – 25 = 80 W m^{-2}.

The parameter F_0 is altered in 4 different sensitivity runs in order to evaluate the effects that different cooling rates have on cloud top entrainment, turbulence, and precipitation. Two of the experimental simulations feature values of F_0 decreased in increments of 20 W m^{-2} so that the radiative cooling is weaker. Similarly, in the other two experimental runs, F_0 is increased in 20 W m^{-2} increments. Together with the control run, the five simulations run have F_0 = 40, 60, 80, 100, and 120 W m^{-2}. While keeping all other parameters identical, this approach isolates the effects that cloud-top radiative cooling has on boundary layer stratocumulus. We note that in the sensitivity experiments, the different values of F_0 may no longer be thermodynamically consistent with the free-tropospheric profiles used in the simulations (which we do not change), but over the 12-hour simulation, the differences in free-tropospheric profiles do not lead to substantial differences in simulation outcomes. Our approach is therefore a controlled and physically plausible way to vary the maximum possible cloud-top cooling.

2.3 Analysis methods of sounding observation data

Radiative transfer calculations using the 207 soundings taken during the VOCALS field campaign are used to bracket the range of cloud-top longwave cooling during that period. In particular, we focus on the magnitude of net longwave flux and how it varies as a function of cloud-top height, temperature and moisture jumps across the inversion, and cloud fraction[1]. Cloud fraction is calculated from 10-minute ship laser ceilometer observations that most closely correspond to the respective sounding times. We acknowledge that this is only one method of estimating cloud fraction, and that different methods can given substantially different estimates (Mechem et al. 2015). The longwave forcing across the cloud-top (*LWF*) is calculated from each sounding using the same Fu and Liou approach for which F_0 is calculated for the simulations. LWC profiles are calculated using constraints from LWP data retrieved from microwave radiometer observations (Zuidema et al. 2005) and cloud-base observations from the ceilometer. These *LWF* values are then weighted by the cloud fraction to represent the mean net flux across the boundary layer (ΔF_n), using a similar weighting method to the shortwave radiation calculations in de Szoeke et al. (2012):

$$\Delta F_n = LWF \cdot cf + LWF_0 \cdot (1 - cf) \quad (3)$$

Here *cf* represents the cloud fraction, LWF represents the longwave flux across the cloud-filled boundary layer obtained from the Fu and Liou radiation calculation, and LWF_0 is

[1] We use the term cloud fraction and cloud cover interchangeably. By these terms we mean the quantity obtained by the vertical projection of clouds in a column.

obtained from a similar longwave flux calculation (taken at the same height at *LWF*) across the corresponding cloud-free boundary layer. We note that the combination of temperature and vapor jump even in the cloud-free boundary layer will result in a net flux jump across the boundary layer.

We explore the covariation of ΔF_n values with cloud fraction and with thermodynamic properties calculated from the soundings. This is done by binning all data into three-hour intervals, which corresponds to the frequency of the radiosonde launches. The 3-h sounding frequency is fine enough to resolve the diurnal cycle, and the large number of soundings taken during the VOCALS campaign ensures that each bin contains no fewer than 15 soundings. Calculations of radiative fluxes from the observed soundings provide constraints for the model values of F_0 and provide an understanding of how the control and sensitivity runs align with the spectrum of observed magnitudes of longwave forcing of boundary layer clouds.

Chapter 3. Results

3.1 Observed characteristics of boundary layer thermodynamic, cloud, and radiation properties from VOCALS

The VOCALS soundings from de Szoeke (2012) show the variability of the marine boundary layer especially with respect to latitude (Fig. 3). The soundings observed over the 80°W –85°W longitude band are warmer and more humid than those over the more eastern 70°W –75°W band, which de Szoeke concludes is mainly due to the SST gradient, which increases toward the west. The sounding used in the Mechem et

al. (2012) simulations and used in our simulations was chosen because it was associated with strongly drizzling conditions and a stratified thermodynamic profile. The cloud-top height of that sounding is 1.6 km, which is near the upper extent of the sampled cloud top height (Z_{ct}) range.

Table 1 displays statistics calculated from the 207 VOCALS soundings and includes the control-simulation sounding. *LWF* represents the difference ('jump') in longwave flux across the cloudy boundary layer, found from profiles calculated using the Fu and Liou method; LWF_0 represents similar calculations assuming no cloud is present. The area-mean net flux (ΔF_n) is calculated from (3) and uses the cloud fraction (*cf*) to scale the cloudy and cloud-free fluxes. Z_{ct} values are derived from each sounding as the minimum temperature, since the cloud top is coincident with the base of the temperature inversion and sharply decreasing moisture profile. Although the cloud-top heights range over a full kilometer, the interquartile range (IQR, the middle 50%) spans just under a quarter of a kilometer showing a very narrow IQR. Only 186 soundings have cloud top heights calculated because the remaining 21 observations are cloud-free. The cloudy *LWF* portion of (3) is not applicable for these 21 cloud-free soundings, meaning that LWF_0 alone contributes to ΔF_n.

Because each simulation assumes an initial 100% cloud cover, we seek the range of *LWF**, which represents the *LWF* from soundings with greater than 50% cloud cover and positive *LWF* (one outlier sounding had *LWF* = 0). This sampling method allows us to focus on the soundings that strongly resemble the initial model conditions in terms of cloud cover. The resulting *LWF** ranges from 38 to 109 W m^{-2}, showing that while they represent outliers, the 40 and 120 W m^{-2} sensitivity simulations nevertheless represent

realistic values for overcast initial conditions. Furthermore, the mean LWF^* is near the control simulation of 80 W m^{-2}. Likewise ΔF_n^* and Z_{ct}^*, represent ΔF_n and Z_{ct} from this same ($cf > 0.5$) sample. By way of comparison, Bretherton et al. (2010) found a range of net longwave cooling values from VOCALS aircraft measurements of 70 to 100 W m^{-2}.

To examine diurnal patterns, soundings are binned into 3-hour intervals in Fig. 4 and separated by longitude. Because of sample size limitations, the full diurnal cycle is only crudely represented. Nevertheless, we notice a systematic diurnal signal in cloud fraction (Fig. 4a) both over the eastern and western portions of the domain, with the mean cloud fraction becoming completely overcast shortly after dawn and reaching a minimum near 60% between sunset and midnight at both longitudes.

Contrasts between the western and eastern boundary layers are more apparent in the $\Delta\Theta$ and Δq_v plots in Figs. 4b,c. Here, $\Delta\Theta$ and Δq_v are measures of boundary-layer stratification and for each sounding are calculated as the values of the upper 25% of the boundary layer subtracted by the values in the lower 25% of the boundary layer. These indices are virtually identical to the decoupling metrics of Jones et al. (2011). The western soundings, which include the sounding used in the control simulation, show relatively warmer and drier upper portions of the boundary layer than the eastern soundings. For the eastern soundings, $\Delta\Theta$ peaks during the late afternoon as solar absorption warms the cloud layer. At this time, moisture is increasingly confined to the surface, presumably a result of the stabilizing influence of solar absorption reducing boundary-layer vertical fluxes. There is no clear diurnal pattern for the western soundings, but an increased vertical moisture gradient (more negative Δq_v) accompanies

increased stability (larger $\Delta\Theta$). The western soundings are more stratified than the eastern soundings, which is consistent with the findings from Bretherton et al. (2010).

Another apparent relationship in Fig. 4, especially noticeable in the eastern soundings, is the inverse correlation between cloud fraction and $\Delta\Theta$ and Δq_v magnitudes. The cloud cover is at its most reduced state when $\Delta\Theta$ and Δq_v are near their greatest magnitudes. This finding suggests that higher MBL stratification and stability are associated with reduced cloud cover, but whether this is a causal relationship is difficult to say solely from this sample of soundings. This relationship will be further examined in the model simulations.

To see how the observed data relates to our longwave forcing (*LWF**) values specified in the model simulations, Fig. 5 bins the soundings with respect to longwave forcing in 10 W m^{-2} intervals. The number of soundings displayed in Fig. 5a show that the sample subset used for the calculations in Table 1 account for nearly the full set of soundings with the exception of the lower net flux ranges where 21 of the 207 soundings are associated with cloud-free conditions. From these sampled soundings, stability and stratification are once again plotted as $\Delta\Theta$ and Δq_v between the upper and lower quartiles of the boundary layer in Figs. 5b and c respectively. With respect to net flux, the sample size again limits what can be concluded about the magnitude of the boundary layer stability. As in the diurnal cycle, when stratified by net flux, the local minimum in $\Delta\Theta$ aligns with the local maximum in Δq_v. The least stable boundary layers are associated with larger values of net flux (with the exception of 110 W m^{-2}, for which there are very few samples), suggesting that a stronger radiative driving of the boundary layer pushes the boundary layer toward a more well-mixed state. The relationship

between cloud-top height and ΔF_n is clear, however (Fig. 5d), and this is presumably a function of longitude. Stronger longwave cooling is associated with greater median cloud-top height, and the variability is small compared to the other plotted properties.

3.2 General results from the model simulations

For the control (80 W m^{-2}) and sensitivity (40, 60, 100, 120 W m^{-2}) simulations, Fig. 6 shows time-series plots of domain averaged cloud fraction, turbulent kinetic energy (TKE), rainfall rate, and precipitation accumulation between 6 and 12 hours. The previous hours are excluded from the plot, as no significant precipitation is occurring in any simulation. As expected, nonzero drizzle rates begin sooner in the runs with stronger radiative forcing (Fig. 6c), and those simulations exhibit the greatest amount of accumulated precipitation (Fig. 6d). Time-series plots show that the rainfall rates for the 120, 100, and 80 W m^{-2} simulations peak almost exactly at 8, 9, and 10 hours respectively, while the 60 and 40 W m^{-2} simulations do not appear to reach a peak within the 12 hour simulation window. Furthermore, TKE values (Fig. 6b) peak simultaneously or just prior to the maxima in precipitation rate, suggesting that the two processes are related. Drizzle rates in Fig. 6b exhibit a self-limiting behavior similar to Burleyson et al. (2013), who found that drizzle-cell area was self-limiting, which they speculate is also reflected in a self-limiting of area-mean drizzle rates. We show in Sec 3.4 that the self-limiting behavior in Fig. 6b is associated with drizzle-induced stabilization of the boundary layer.

Stronger radiative cooling helps sustain an overcast boundary layer (Fig. 6a). The cloud fraction of the 40 W m^{-2} simulation begins to decline as soon as 5 hours into the

simulation and decreases to 70% by 12 hours. Meanwhile, the remaining simulations all show nearly 100% cloud coverage until around 8 hours when cloud fraction in the 60 and 80 W m^{-2} simulations begin to decline. At this time, cloud fractions from the 100 and 120 W m^{-2} simulations exhibit slight variations but still hover near completely overcast conditions. This result of stronger radiative forcing promoting cloud cover runs counter to the notion that turbulence driven by cloud-top cooling is known to dry the cloud layer (Krueger et al. 1995). We address this apparent paradox in Sec. 3.3 below.

Horizontal cross sections of column-maximum (composite) reflectivity and liquid water path are plotted closest to the time of maximum mean surface precipitation rate for each simulation (Fig. 7). These horizontal cross sections suggest that maximum rainfall rates across the model domain are greater in the runs with higher radiative forcing, not because the precipitation cores are significantly more intense but rather because they are more widespread (i.e., cover greater area). The frequency distribution of surface drizzle rate plotted in Fig. 8 confirms the visual impression from the reflectivity and LWP fields. The distributions in Fig. 8 are normalized such that the area under the curve is proportional to drizzle area, indicating that the more strongly forced cases have greater drizzle area (similarly, the first moment of the distribution is proportional to mean drizzle rate). All the cases except the most strongly forced one exhibit similar distribution shapes and modal frequency. These two results together demonstrate that the character of the precipitating regions is similar across all the simulations but that the precipitation area increases with forcing. The increase in precipitation with increasing forcing arises from increases in precipitation area rather than increased precipitation intensity in the drizzling regions. The most strongly forced case (120 W m^{-2}) is somewhat different in that its

modal frequency is shifted toward smaller drizzle rates, although it does exhibit the largest precipitation area of all the simulations.

3.3 Analyzing up and downdraft core fraction vs. strength

Distributions of the vertical velocity for the control (40 W m^{-2}) simulation are plotted in Fig. 9 in the form of contoured frequency by altitude diagrams (CFADs, Yuter and Houze 1995). These CFADs provide insight to what altitudes contain the strongest updrafts and downdrafts. The four panels in Fig. 9 display the vertical distributions for hour-long intervals beginning with the 3rd hour, which immediately follows the completion of the spin-up time, through the 6th hour (6–7 h) after which precipitation begins to significantly increase. The gray horizontal dashed lines in each panel represent the domain-averaged cloud top and base heights.

The hourly progression of the vertical velocity distributions between the end of spin-up and start of precipitation periods help show the nature of the turbulence transition in the control simulation. Early on, the stronger vertical motion is dominated by entrainment-driven downdrafts near the top of the boundary layer, but as the cloud base lowers, updrafts originating closer to the surface begin to play are more prominent role. Eventually, the cloud layer becomes dominated by updrafts that greatly exceed the strength of the downdrafts. It should still be noted however, that the magnitude of these upper-level downdrafts only slightly diminishes, while the extent of the stronger downdrafts expands toward the surface, showing that the overall turbulence of the boundary layer increases over time, just more noticeably within the updrafts.

To supplement the vertical velocity results shown in these vertical velocity CFADs, profiles of updraft and downdraft mass flux (Fig. 10) are conditionally sampled at different thresholds of vertical velocity, as in Mechem et al (2010). This contour plot illustrates the contributions to the total mass flux from updrafts and downdrafts of selected magnitudes between simulation hours 9-11, during which the precipitation rates peak. The overall updraft and downdraft contours ($w>0$, $w<0$) are mirror images, consistent with conservation of mass within the model domain. While the downdrafts contributing to the mass flux are predominately weak, the updrafts are characterized by many cores with much stronger vertical velocities, particularly in the cloud layer. These strong updraft cores likely contribute to the bulk of the precipitation as they are most prevalent right before rainfall rates begin to increase (Figs. 6d, 9).

To gain a better understanding of the mechanisms leading the formation of these precipitation cores, we explore mean-vertical profiles for each simulation averaged over a 2-hour time window centered on the time of maximum precipitation for each simulation. This yields time windows of 7-9, 8-10, and 9-11 hours for the 120, 100, and 80 W m^{-2} profiles, respectively, and 10-12 hours for the 60 and 40 W m^{-2} profiles.

The domain-averaged profiles in Fig. 11 show that during each averaging period, the boundary layer is deepest in the simulations with the strongest radiative cooling. In this figure, the intermediate simulations (60 and 100 W m^{-2}) are excluded to avoid clutter. Moreover, we note that the 60 W m^{-2} profile lies between the 40 and 80 W m^{-2} profiles, and the 100 W m^{-2} profile lies between the 80 and 120 W m^{-2} profiles, so the progression of the profiles from 40–100 W m^{-2} is largely monotonic. The differences in radiative cooling strengths between the simulations are evident in the cloud-layer potential

temperature (Θ_l). The lower Θ_l values near top of the boundary layer in the 120 W m^{-2} simulation are indicative of stronger radiative cooling and suggest an environment that serves to enhance buoyancy for surface-based updrafts, relative to more weakly forced cases where the cloud layer is warmer. All three q_t profiles (Fig. 11b) are similar in the cloud layer, but the 40 W m^{-2} simulation has q_t values that are ~1 g kg^{-1} greater over the subcloud layer. We interpret these differences as a combination of the stronger radiative forcing enhancing entrainment-drying but also more completely mixing the surface moisture flux throughout the boundary layer. Because of the weaker vertical fluxes in the weakly forced case (40 W m^{-2}), a surplus of moisture is restricted to the subcloud layer and cannot contribute to in-cloud processes. The sharp decline in q_t near 0.4 km, also described in Mechem et al. (2012), allows each simulation to be formally categorized as "decoupled," at least in terms of moisture stratification. The variation in radiative forcing across the simulations leads to a continuum of stratification. These mean profiles show that stronger radiative forcing indeed dries the total water in the cloud layer (Fig. 11b), but the cooling of the cloud layer (Fig. 11a) is sufficient to change the saturation mixing ratio in such a way to result in an increase of cloud water (Fig. 11c). This behavior is somewhat different than the conceptual model of turbulence driven by longwave cooling drying the cloud layer (Krueger et al. 1995).

Varying longwave forcing most directly influences the vertical motion and the buoyancy-generation of turbulence (buoyancy flux). Figures 11d-f show the vertical velocity characteristics between the simulations during their periods of peak rainfall intensity. Increased turbulence (as portrayed in the vertical velocity variance profiles) is evident in the runs with stronger radiative forcing, especially in the cloud layer. The

positive vertical velocity skewness profiles in Fig. 11e imply that the circulation tends to be dominated by strong, narrow updrafts and broad, weaker downdrafts, which suggests bottom-up, surface-based dynamics. Surface-based convection is consistent with the stratified thermodynamic profile, which has been shown in LES studies (e.g., Stevens et al. 1998). Meanwhile, near the surface, the slightly negative skewness in the 120 W m^{-2} simulation is likely a result of strong, evaporatively cooled downdrafts. Profiles of the buoyancy flux ($\rho c_\rho \overline{w'\theta_v'}$) in Fig. 11f show buoyancy-generation of TKE over the entire boundary layer, with the exception of the entrainment region at cloud top. The local minima in buoyancy flux near cloud base likely result from the stability that parcels experience when cloud-layer downdrafts penetrate into the subcloud layer (or similarly, when subcloud-layer updrafts rise into the cloud layer). For the majority of the boundary layer, stronger buoyancy fluxes correlate positively with radiative forcing, but the relative roles that the vertical velocity and buoyancy itself play in this buoyancy flux are uncertain.

To determine whether the differences in buoyancy flux and vertical velocity across simulations result from differences in core strength or differences in the number of cores as suggested by the reflectivity plots, we further conditionally sample the fields used to calculate the profiles in Fig. 12. The positive vertical velocity skewness of each simulation as seen in Fig. 11e suggest the importance of updraft cores, so we isolate positively buoyant cloud cores during each simulation's period of peak precipitation (cloud-core excess of virtual potential temperature or "buoyancy excess" [K], $B = \theta_v' - \overline{\theta_v}$). The profiles in Fig. 12 are sampled over grid locations that have cloud liquid water (>0.01 g kg^{-1}) and are and positively buoyant ($B > 0$).

The cloud core area fractions (Fig. 12a) are greater in the runs with stronger radiative forcing. This finding is consistent with the perspective of Figs. 7 and 8 that the increased precipitation in the more strongly forced runs result largely from an increase in precipitation area. Meanwhile, differences between simulations are more subtle in the vertical velocity profiles (Fig. 12b) at the altitudes in with the highest core fractions, but there is still a weak but noticeable increase cloud core *w* accompanying the increased radiative forcing. Although differences in core precipitation rates are negligible between simulations, the rate at which these cores ascend is slightly faster when radiative cooling is stronger, and these differences in ascension rate likely are likely associated with differences in turbulent intensity across the simulations. We note that the cloud core *w* is small over the cloud layer. This results from the characteristics of the cloud layer in which the updraft cloud fraction is large (Fig. 12a) but for the most part dominated by small, weak updrafts, which overwhelm the large, strong updrafts in calculating the mean core *w*.

The virtual temperature excess profiles in Fig. 12c align similarly to the vertical velocity profiles in that the 120 W m^{-2} shows the most strongly buoyant parcels at the mid levels of the MBL. This result shows a relationship between larger buoyancies and faster vertical velocities. Although the core fractions at the mid-levels are small for all simulations, the more strongly forced cases with larger buoyancies and vertical velocities are able to transport larger amounts moisture to the upper levels of the boundary which likely influences the increased core fractions near the cloud top.

3.4 Analyzing the roles of [top-down vs. bottom-up] turbulent mechanisms

To further quantify the impact of radiative forcing on the development of surface-driven updrafts and the subsequent effects on precipitation and cloud cover, we must examine in detail the evolution of the boundary-layer cloud and turbulence properties. It is possible that increased longwave cooling simply leads directly to enhanced turbulence and stronger precipitation. However, the simulation results suggest that the strong stability tends to suppress the generation of strong, negatively buoyant downdrafts from longwave cooling. The mass flux contributions and skewness profiles indicate that the strongest buoyancy-driven flows are updrafts, which are predominantly surface-based, and the conditionally sampled cloud core profiles indicate that these surface-based updrafts are stronger when cloud-top radiative cooling is increased. What is unclear however, is the specific mechanism(s) through which increasing cloud-top longwave cooling leads to more prevalent and stronger surface-based updrafts.

Figure 13 shows the time-evolution of vertical velocity variance, buoyancy flux, and skewness for the 40, 80, and 120 W m^{-2} simulations. Figure 13a shows that early in each simulation, turbulence is confined toward the top of the boundary layer, with additional weak turbulence near the surface, suggesting two distinct MBL circulations (decoupling). As expected, the analyses with stronger radiative forcing experience stronger and deeper vertical velocities, and each simulation's vertical velocities peak during their respective periods in which they produce the majority of their precipitation (cf. Figs. 13 and 6). Noteworthy in Fig. 13a is how the highest vertical velocities remain near the top of the boundary layer and gradually extend downward into the subcloud layer. One possible explanation for this behavior is that the longwave cooling-driven downdrafts increase in strength and thereby impact a deeper layer as each simulation

progresses. This perspective is consistent with the ship-based cloud-radar observations of Burleyson and Yuter (2013, their Fig. 2) who argue that, as the night progresses, radiatively cooled downdrafts penetrate lower and lower and eventually are able to reach the enhanced low-level moisture and mix it upward to provide a moisture source for the cloud.

The buoyancy flux in Fig. 13b indicates TKE generation in both the cloud layer and at the surface, with both mechanisms becoming stronger in the more strongly forced cases. The buoyancy flux also peaks slightly earlier than the vertical velocity for each simulation, which is consistent with buoyancy-driven updrafts. The vertical velocity skewness in Fig. 13c further reinforces the idea that surface-driven updrafts are the predominant turbulent mechanism when precipitation is present. The beginning hours of each simulation show large negative w' skewness, indicative of narrow, radiatively driven downdrafts. When precipitation begins to occur in each simulation, the skewness quickly transitions to positive, which corresponds to a radical change in circulation dynamics, as the downdraft-dominated dynamics transition to updraft-dominated. The positive skewness and the strong, cloud-level vertical-velocity variance are consistent with the prevalence of buoyant, surface-based updrafts that gain momentum as they rise. We note that the precipitation is not the cause of the transition but rather an effect of increased turbulence (updrafts and downdrafts) driving the precipitation process.

Figure 14 shows the evolution of the boundary layer temperature and liquid content profiles to illustrate the evolution of stratification over the course of the simulation. Our discussion focuses on the 80 W m^{-2} control simulation; the other simulations are qualitatively similar but transition more slowly (40 W m^{-2}) or more

quickly (120 W m^{-2}). Before significant precipitation occurs prior to 8 h (Fig. 6d), the boundary layer below 0.5 km warms and becomes less stable (i.e., the vertical gradient of Θ_l weakens). Similarly, over time the cloud layer becomes less stable (i.e., closer to being well mixed), as longwave cooling acts to drive turbulence that homogenizes the thermodynamic properties in the vertical. Because of the lack of deep-layer circulations over the first 8 hours of the simulation, surface latent heat flux results in a build-up of moisture at lower levels. The lack of deep updrafts precludes the transport this moisture up to the cloud layer, which is drying over time from entrainment of free-tropospheric air. Even after the subcloud and cloud layers are destabilized, there remains a stable layer in the 500–700-m layer that inhibits whole-scale overturning of the boundary layer. This destabilization of the subcloud and cloud layers, however, preconditions the atmosphere for circulations that span the depth of the boundary layer.

The behavior of the simulations seem broadly consistent with the transition evident in the 3-hourly composite from Burleyson et al. (2013, Fig. 3). It is difficult from the 3-hourly averaging period of the composite to evaluate the timescale of the simulated transition in detail, but the structural details and the timescale of the evolution are qualitatively similar. The observed boundary layer from VOCALS is most strongly stable in the mid-afternoon. The boundary layer destabilizes overnight, although there is strong evidence of localized stabilization (their Fig. 11) in the midnight-to-sunrise timeframe associated with the previously discussed drizzle self-limiting. The transition is even more evident in the composite moisture profiles (their Fig. 3), which exhibit a pronounced transition from highly stratified to less decoupled (though not perfectly well-mixed). The simulations show that destabilization is not immediate and takes time after solar heating

is reduced. In the control simulation (Fig. 14a), the cloud layer is rendered well-mixed after ~6–8 h, but the stable layer from 500–700-m is never completely eroded (evident from the buoyancy flux minima in Fig. 11f). This timescale appears to be roughly consistent with the VOCALS observations. Additionally, the joint behavior between the self-limiting drizzle and stability in Burleyson et al. (2013) is well represented in the simulations.

The beginning of precipitation at 8 h in the control simulation is accompanied by updrafts rooted near the surface (Fig. 13), ultimately leading to a stabilization of the temperature profile and a return of the moisture profile back nearly to the initial state (Fig. 14). The boundary layer is stably stratified and dominated by surface-based updrafts. By measure of stratification alone, we might consider it decoupled, but the deep convective transports along with the positive buoyancy flux, even through the stable subcloud region, suggests a more apt description of "coupling by deep cumulus updrafts." The stratification of the moisture and temperature fields is easily seen in time series of the thermodynamic variables in Fig. 15a and b. (As previously stated, these quantities are equivalent to the decoupling metrics of Jones et al. 2011).

The Buoyancy Integral Ratio (BIR) in Fig. 15c provides another measure of decoupling in each simulation. BIR gauges the importance of negative buoyancy flux in the subcloud layer, relative to the total buoyancy flux. The equation for BIR defined by Bretherton and Wyant (1997) can be expressed as:

$$BIR = -\int_{z<zb,(w'\Theta_v')<0} (w'\Theta_v')dz \Big/ \int_{All\ other\ z} (w'\Theta_v')dz \quad (4)$$

Bretherton and Wyant (1997) found that higher BIR values equate to stronger decoupling indicating that entrainment-driven turbulence is the dominant mechanism within the boundary layer. A line is plotted at 0.15 to show the Bretherton and Wyant (1997) threshold of which an exceeding *BIR* value indicates a decoupled boundary layer. With the exception of the 40 and 60 W m^{-2} cases, each simulation's *BIR* plateaus near 0.15 around the 3-hour mark after the spin-up time is complete and remains near that level until precipitation occurs, driven by a strengthening of turbulence. Prior to precipitation, most of the simulations lie near the BIR threshold of decoupling. Within each simulation, the boundary layer begins to re-couple (as evident by decreasing BIR values in Fig. 15c), which is associated with an increase in buoyancy flux, skewness (as seen in Fig. 13), and precipitation (as seen in Fig. 6). As for the 40 and 60 W m^{-2} cases, the sharp BIR increase prior to precipitation may be the result of negative fluxes brought about by the increasing vertical motion at that time (from 8–11 h) acting on the stable layer.

Chapter 4. Discussion and Conclusions

Using a well-known idealized parameterization of longwave-cooling, we are able to vary the net longwave flux (ΔF_n) across the boundary layer and isolate the impacts of radiative cooling on entrainment rates, MBL decoupling and stability, cloud-top heights, cloud coverage, precipitation, mesoscale organization, and the relative roles of top-down vs. bottom-up turbulence-generation mechanisms. Meanwhile, longwave radiative transfer calculations on data from the observed VOCALS soundings help to constrain the sensitivity experiments by showing that the range of ΔF_n values used in the sensitivity

cases are present over the Southeast Pacific. We are limited in making additional conclusions about relationships between ΔF_n and other MBL properties not available from solely the observed sounding observations. We also acknowledge that a substantial portion of the soundings are influenced by daytime shortwave heating of the cloud layer, which may exert some influence on the longwave flux calculation due to heating and drying of the cloud. The simple longwave flux parameterization neglects cooling in cloud-free regions that has been argued to sometimes be important (Wang and Feingold 2009a).

In a general sense, all simulations exhibit an initially stratified MBL dominated by top-down, buoyancy-circulations that transition to bottom-up, surface-based turbulence responsible for producing the bulk of the precipitation. This transition initiates when negatively buoyant downdrafts along with weak surface fluxes destabilize the MBL leaving only a shallow inversion layer spanning from roughly 500-700m elevations. This process is evident in the layer of downdrafts penetrating lower and lower until reaching a point where the moisture trapped by the stratification is able to be transported upward into the cloud by these downdrafts and subsequent surface-based updrafts. Although this stable layer never fully mixes out, the stronger surface-based updrafts are able to penetrate this layer and are then aided in their ascent by increased buoyancy once they enter the cloud layer.

The simulations differ in how the magnitude of radiative cooling influences the timing and intensity of this transition. In the more strongly forced runs, the increased top-down turbulence more quickly preconditions the environment for the onset of surface-driven fluxes. The earlier onset is accompanied by increased overall bottom-up

turbulence leading to greater overall precipitation and a more sustained cloud cover because of enhanced vertical moisture transport from low levels. All simulations produce sufficient entrainment to dry the cloud layer, and only the stronger ΔF_n values are actually capable of bringing about transports (both updrafts and downdrafts) that fully replenishing the moisture to the upper MBL, thereby maintaining complete cloud coverage.

Although the *TKE* and precipitation amounts increase with ΔF_n, the precipitation rates within these updraft cores are relatively similar for all cases. Although surface-based parcels from the more strongly forced simulations that penetrate the inversion layer rise through the cloud layer at slightly faster velocities and with slightly increased buoyancy, the increased precipitation amounts can be predominantly attributed to the overall increase in the areal extent of the updraft and precipitation cores. The enhanced destabilization from the more strongly forced runs allows these cores to break through the 500-750-m stable layer more easily. Surface-based convection in each simulation occurs once the instability measure $\Delta\theta$ decreases below some threshold magnitude. Convection is initiated sooner and is stronger and more widespread in the simulations with stronger longwave forcing (larger ΔF_n). The stability time-series plots in Fig. 14 suggest that this threshold may be similar throughout each simulation. For all cases except the 40 W m^{-2} case, $\Delta\Theta_l$ values reach a minimum around 2 K. All simulations have Δq_t values reach values of –3 g kg^{-1}. *BIR* values plateau around 0.15 in each case with the exception of the 40 and 60 W m^{-2} simulations in which the cloud cover begins to diminish. Precisely identifying and quantifying the threshold leading to surface-based convection, and whether or not it varies with ΔF_n, will be a key component of future research.

Simulation results exhibit similarities to observations from field campaigns. Ship-based data from the VOCALS field study in Burleyson et al. (2013) shows precipitation peaking a few hours before sunrise, the boundary layer decoupling over the course of the daytime hours, and then beginning the process of recoupling near sunset. Our simulations are most concerned with this recoupling process, as the boundary layer transitions out of its decoupled state. The simulations produce a coupling through cumulus transports, but the dynamics remains predominantly surface-based, as opposed to being predominantly driven by cloud-top cooling. This may be due, at least in part, to the proclivity of this case setup to produce substantial drizzle, which will push the boundary layer toward decoupling.

As a highly idealized numerical study examining the sensitivity of drizzling stratocumulus to large differences in longwave forcing, the simulation results can be put in context with cloudy boundary layers from other cases or different stratocumulus regions. From an observational standpoint, the ranges of ΔF_n calculated from the VOCALS soundings can be compared to other field studies such as the FIRE or DYCOMS-II campaigns. With the appropriate sampling, the relationships between radiative forcing and the subsequent turbulent mechanisms seen in the model results can be more strongly compared to actual data including sounding profiles, cloud cover, and precipitation measurements. From the modeling standpoint, simulations can further investigate the nocturnal transition of MBL turbulence from being top-down to bottom-up dominated. In addition to characterizing the stability threshold that leads to this switch of mechanisms, this transition can be explored in many more aspects beyond its relation to radiative forcing. Ideally, parameterizations used to represent these clouds in

numerical weather prediction and global climate models should be able to represent these different dynamical boundary-layer behaviors.

Appendix

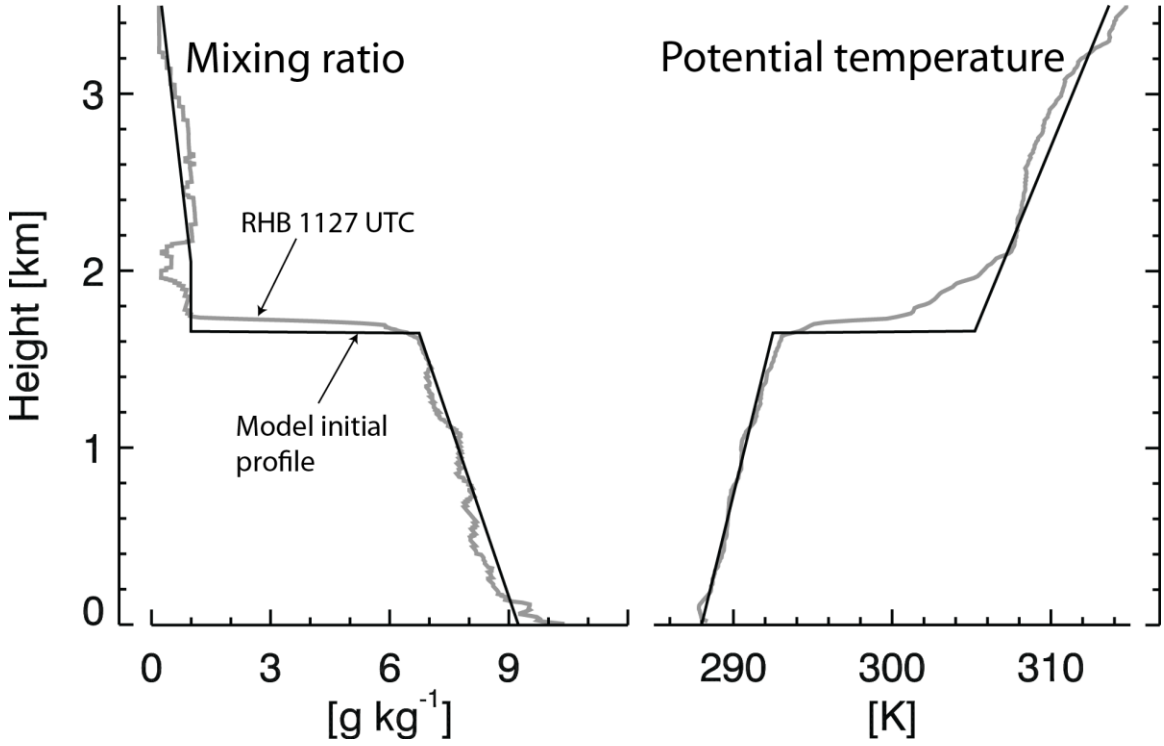

Figure 1. Idealized soundings used for the LES initial conditions overlaid on the sounding launched from the RHB at 1127 UTC (0527 LT) 26 October 2008 near 19.6°S, 85.8°W (adapted from Mechem et al. 2012).

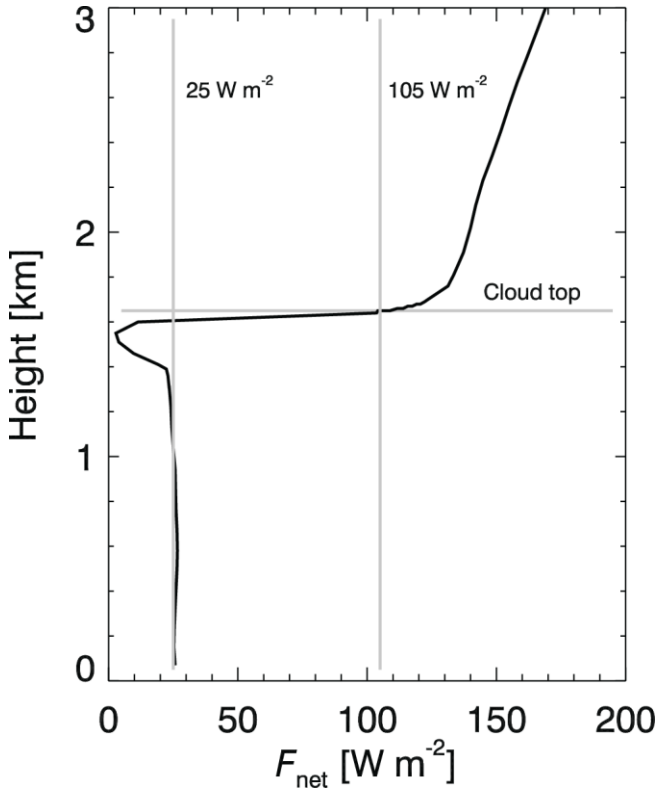

Figure 2. Vertical profile of the net longwave radiative flux employed calculated from the sounding in Fig. 1 and assuming a simple adiabatic liquid water profile as described in the text (Mechem et al. 2012).

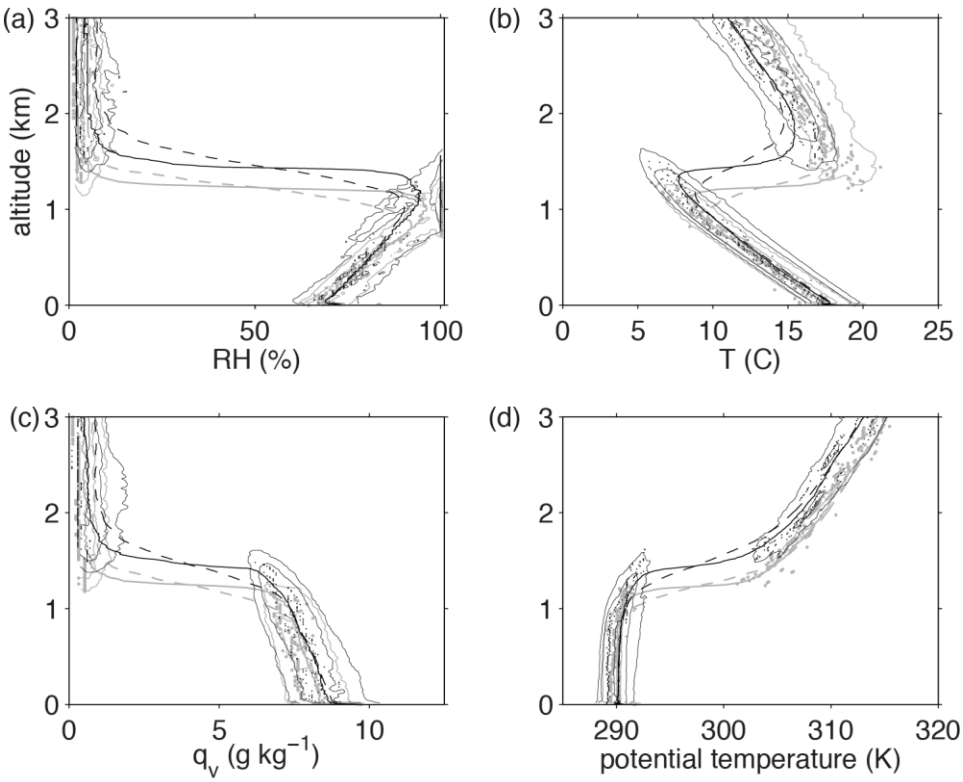

Figure 3. Compilation of soundings along 20°S taken from the VOCALS regional experiment. Data from 75°W–80°W are in gray while data from 80°W–85°W are in black. Dots correspond to the distribution mode for each vertical level. The solid and dashed lines represent the median and mean, respectively. Contours represent 1/8, 1/4, and 1/2 of the maximum frequency of occurrence. Figure is taken from de Szoeke et al. 2012.

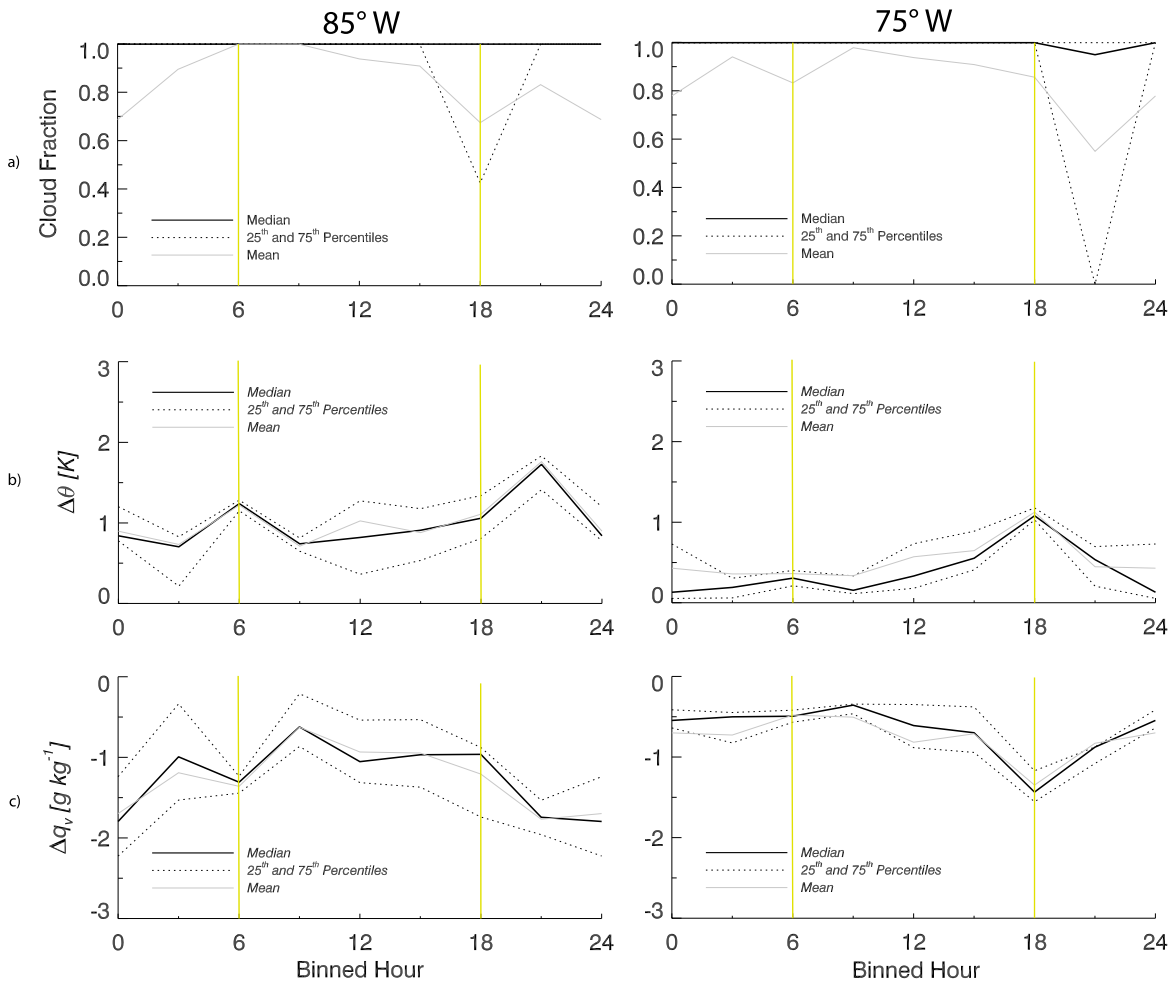

Figure 4. All 207 VOCALS soundings and ship-based estimates of cloud fraction, binned in 3-hour intervals [LT]. Median, mean, and 25th and 75th percentile are shown for different quantities. The vertical yellow lines denote the beginning (0600 LT) and end (1800 LT) of daylight hours.

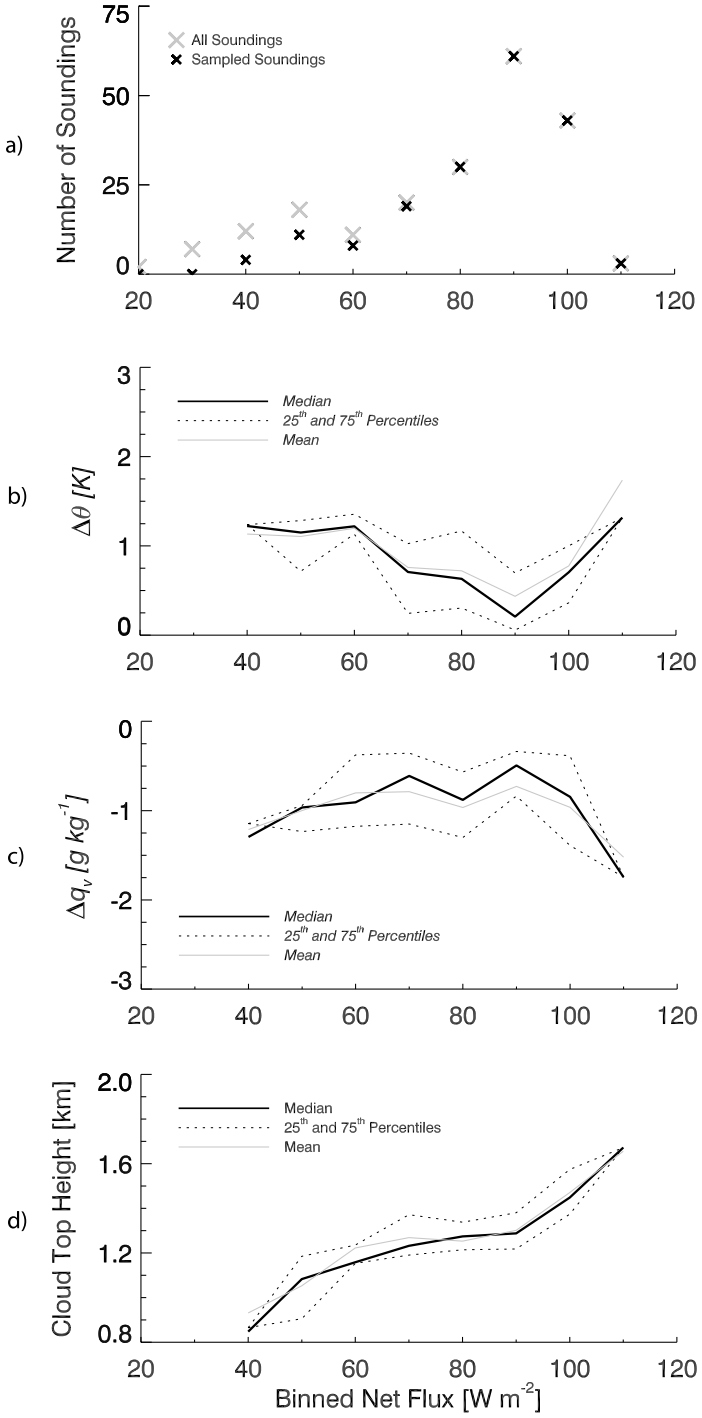

Figure 5. (a) Number of VOCALS ship-soundings binned into intervals of 10 W m^{-2} net longwave flux calculated (ΔF_n) from the Fu and Liou approach. Panels (b) and (c) correspond to differences of liquid water potential temperature and total water between the upper and lower parts of the boundary layer (an indication of stratification or decoupling), also binned by net longwave flux. Panel (d) shows the cloud-top height as a

function of net flux. Panels (b)-(d) show median, mean, and 25th and 75th percentiles of the distributions.

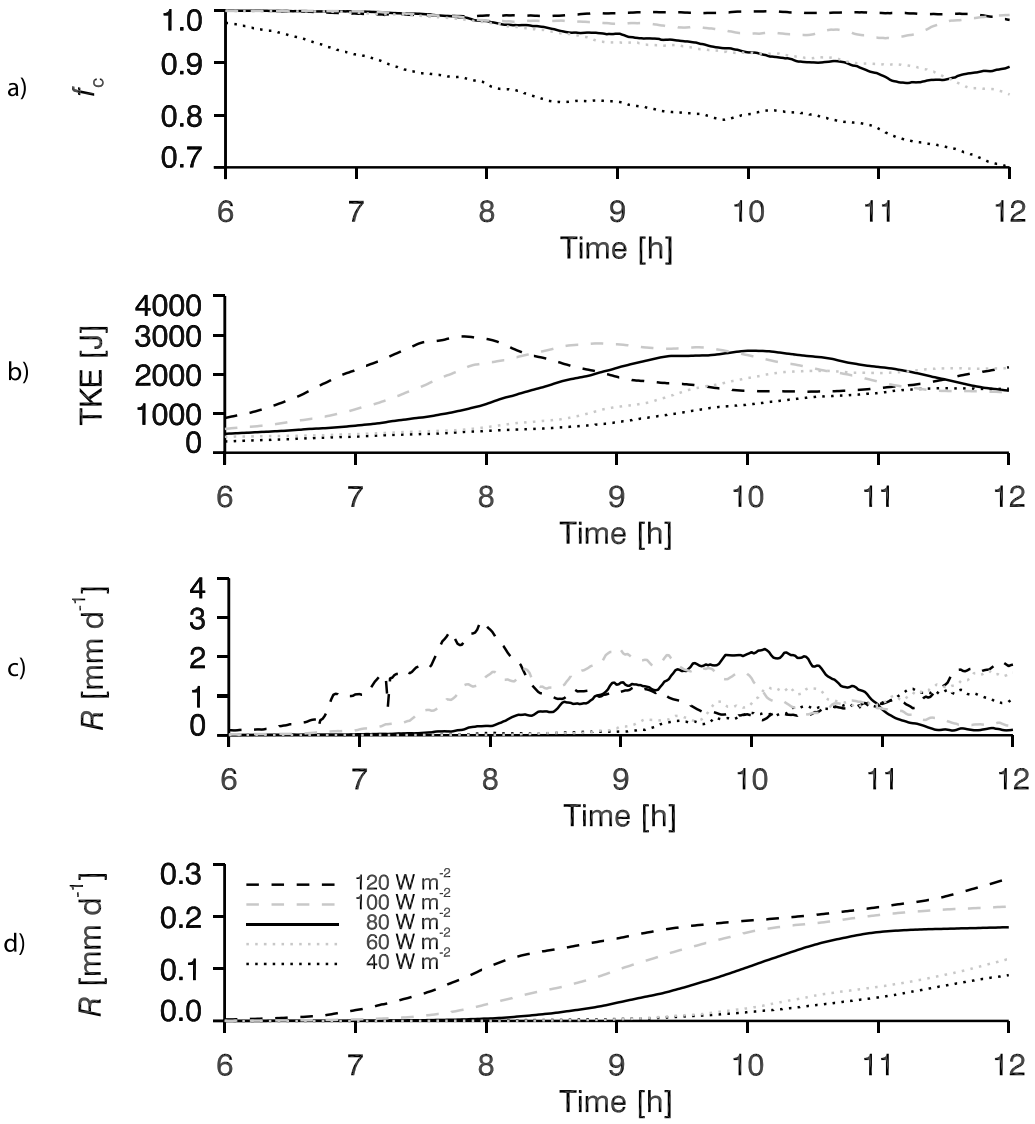

Figure 6. Time-series plots of domain averaged a) cloud fraction, b) turbulent kinetic energy [integrated over the MBL depth], c) rainfall rate, and d) rainfall accumulation for each simulation.

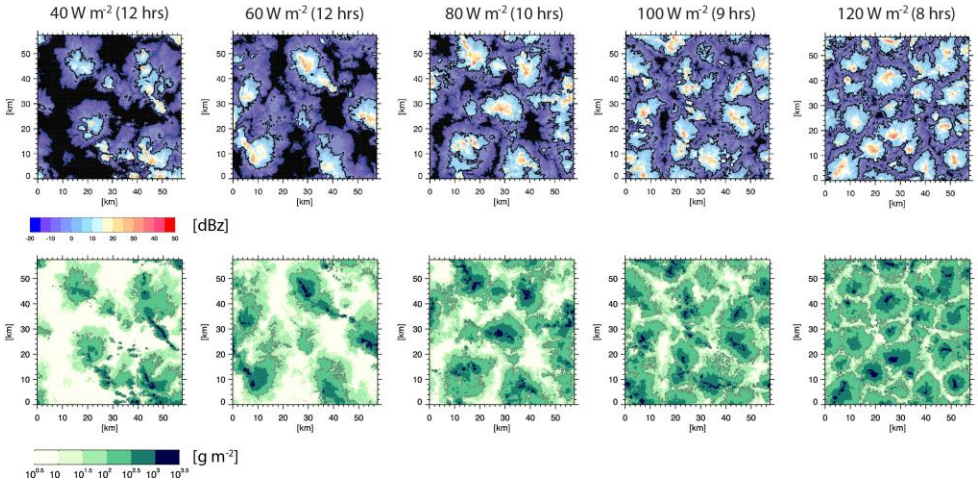

Figure 7. Composite (column maximum) model reflectivity (top) and liquid water path (bottom) taken in the vicinity of the time of peak precipitation intensity for each simulation. The dark black contours on the model reflectivity plots correspond to reflectivity values of 0 dBz, which roughly corresponds to the sensitivity of the C-band precipitation radar deployed on the RHB during the VOCALS campaign.

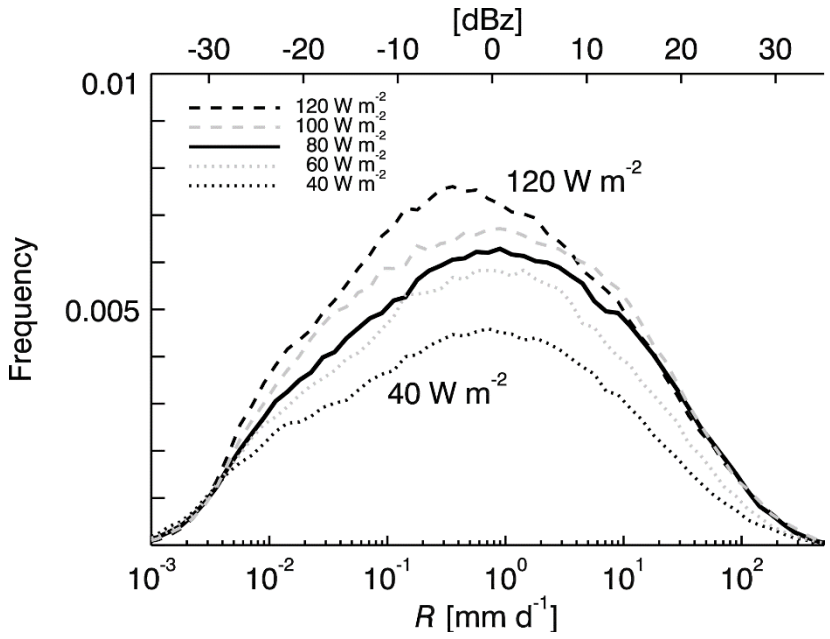

Figure 8. Frequency distribution of surface drizzle rate over the 2-hour window approximately centered on maximum precipitation rate in the five simulations (7–9-h, 8–10-h, and 9–11-h windows for the 120, 100, and 80 W m^{-2} profiles, respectively, and 10–12-h windows for the 60 and 40 W m^{-2} profiles). The distributions are normalized such that the integral with respect to drizzle rate gives a drizzle area fraction (conditioned on areas greater than 10^{-5} mm d^{-1}), so greater area under the curve directly corresponds to greater drizzle coverage. Similarly the first moment of the distribution is related to mean drizzle rate. The reflectivity axis on the top corresponds to a $Z(R)$ relation, with parameters derived from the bin LES output ($Z = aRb$, where a = 73.3 and b = 1.25, and R is precipitation rate in mm h^{-1}. This is merely for comparison; we are certainly not suggesting yet another Z–R relation.)

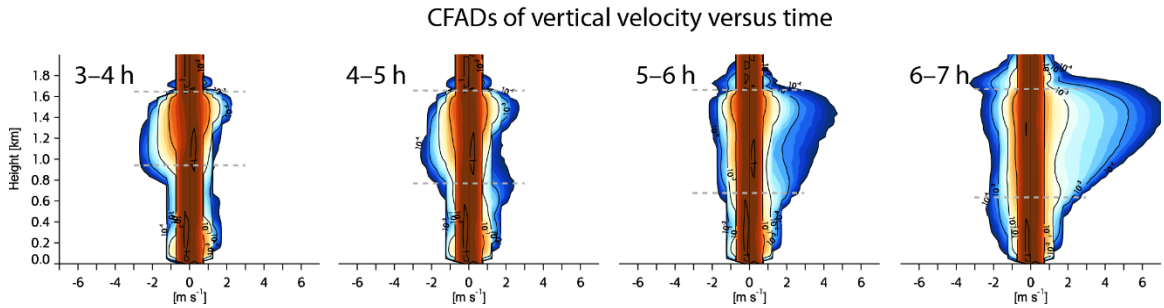

Figure 9. Vertical velocity contoured frequency by altitude diagrams (CFADs) for the control simulation (80 W m^{-2}). Horizontal dashed lines represent mean cloud-top and cloud-base during each period.

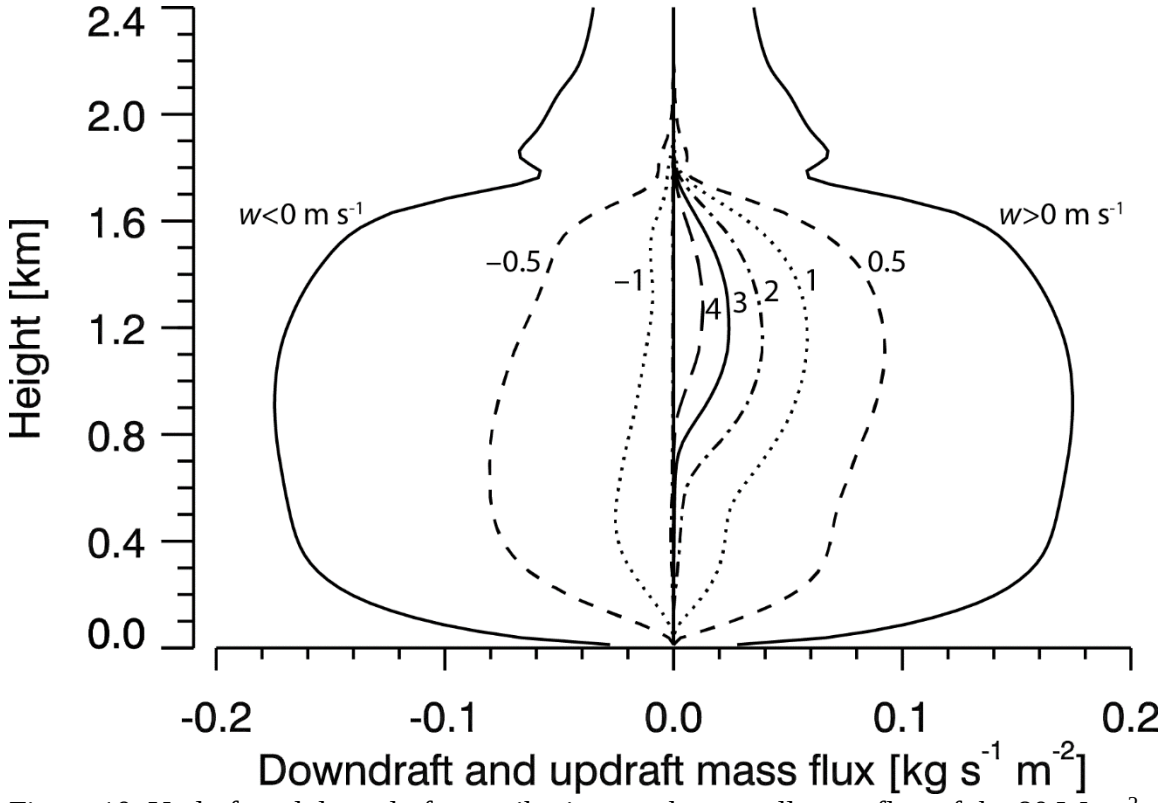

Figure 10**.** Updraft and downdraft contributions to the overall mass flux of the 80 W m^{-2} case, contoured by magnitudes of vertical velocity with respect to altitude.

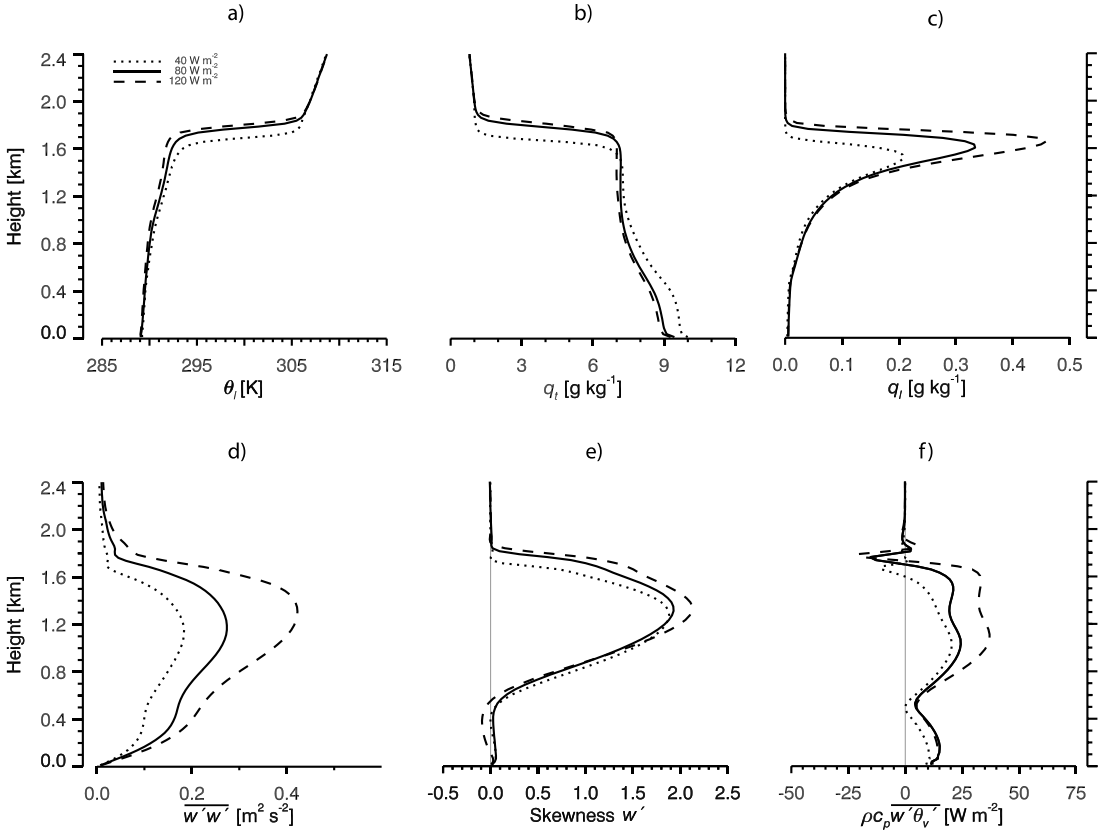

Figure 11. Mean vertical profiles (horizontally averaged over the domain and time-averaged over a 2-hour period around the time of maximum precipitation, as identified in the text) for the 40, 80, and 120 W m^{-2} simulations. a) liquid water potential temperature, b) total water mixing ratio, c) liquid water mixing ratio, d) vertical velocity variance, e) vertical velocity skewness, and f) buoyancy flux.

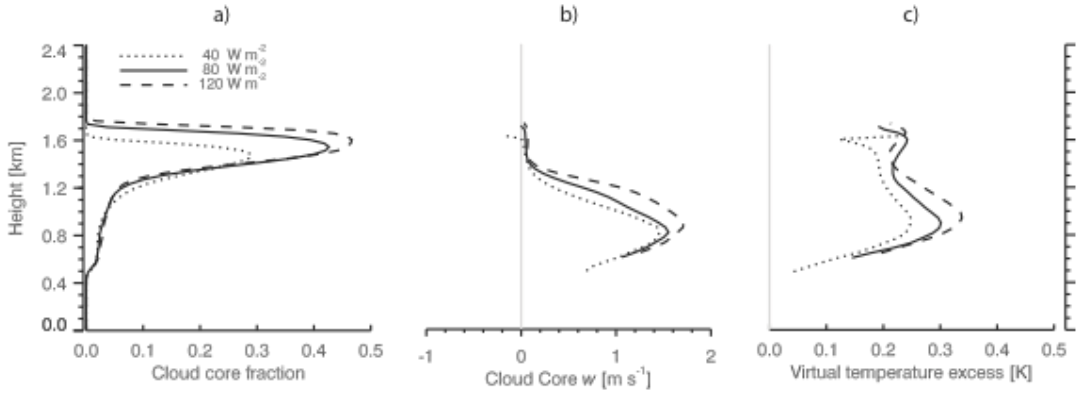

Figure 12. Mean vertical profiles conditionally sampled on positively buoyant cloud cores. (a) Area fraction of positively buoyant cloud cores. (b) Mean vertical velocity in positively buoyant cloud cores. (c) Buoyancy excess in positively buoyant cloud cores.

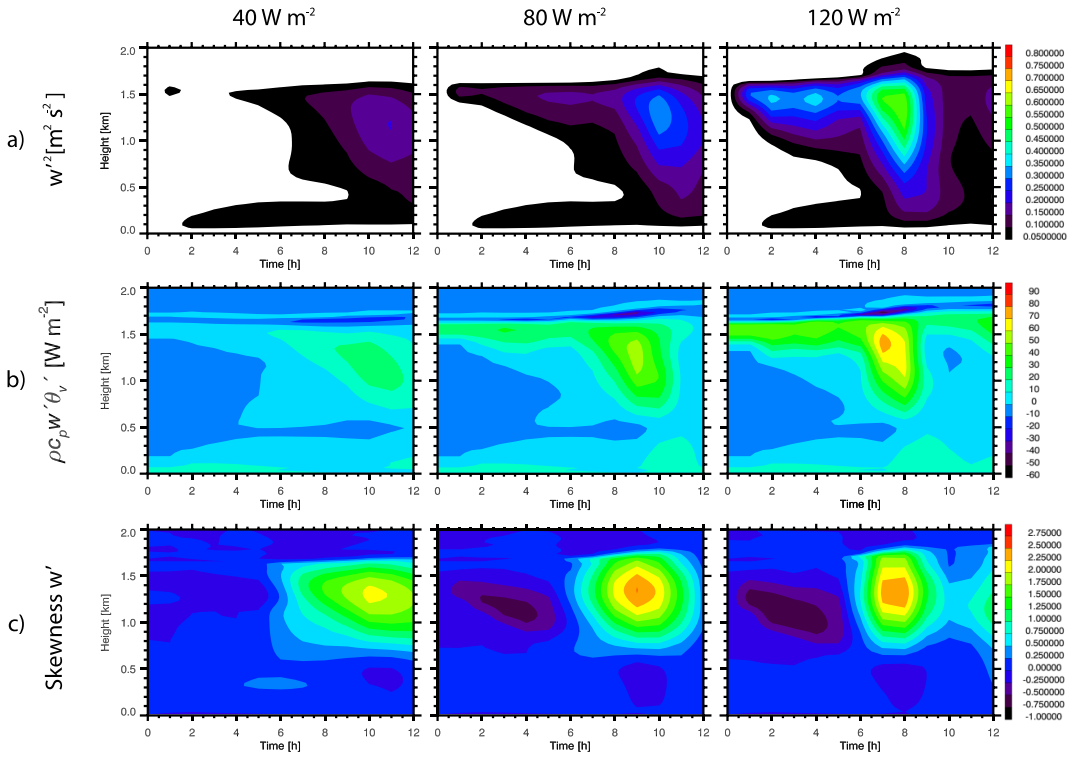

Figure 13. Contoured plots of time vs. height showing vertical profiles of a) vertical velocity variance, b) buoyancy flux, and c) skewness of vertical velocity for the 40, 80, and 120 W m^{-2} simulations.

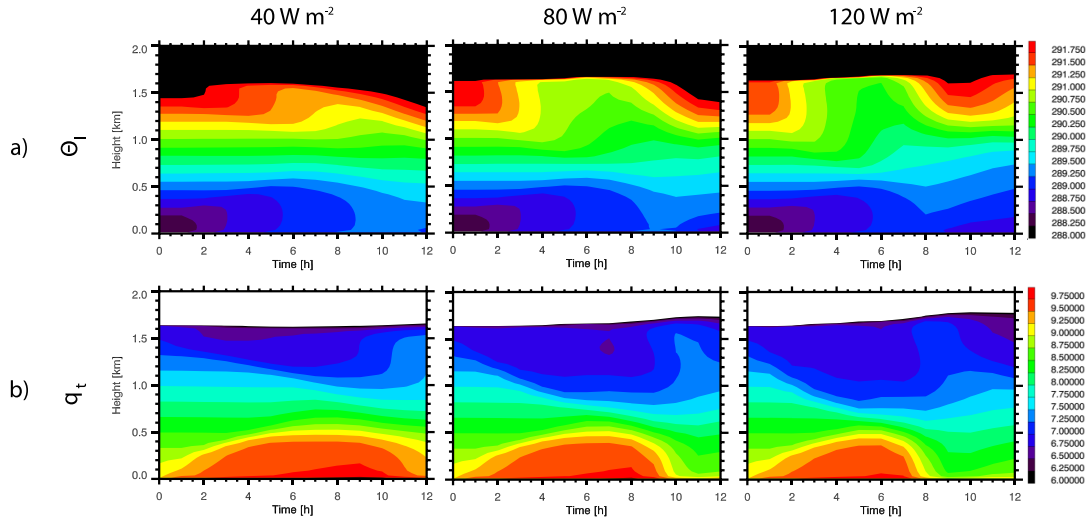

Figure 14. Contoured plots of time vs. height showing vertical profiles of a) liquid water potential temperature and b) total water mixing ratio for the 40, 80, and 120 W m^{-2} simulations.

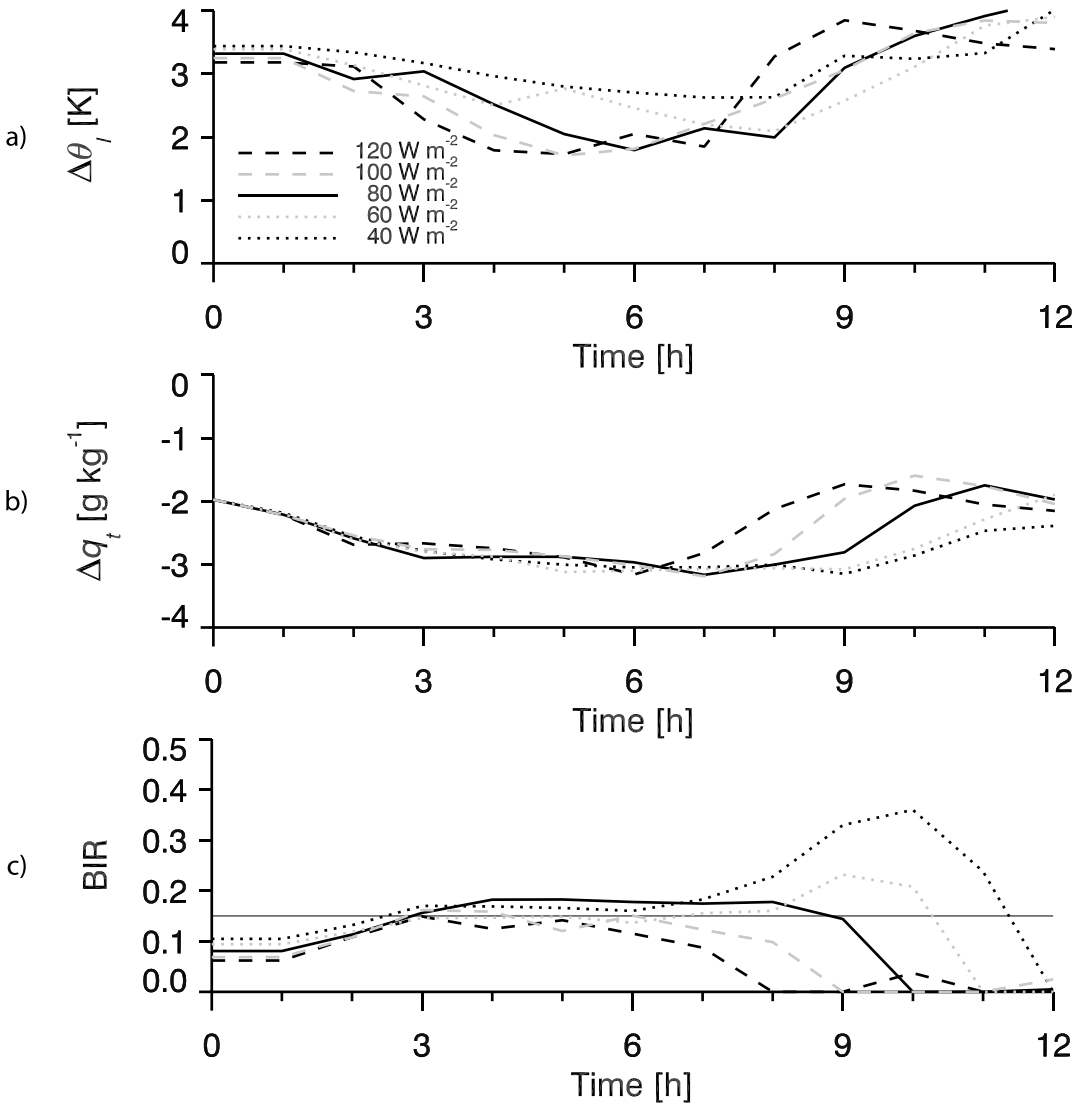

Figure 15. Time-series of boundary layer stratification and decoupling measures. Differences of (a) liquid potential temperature and (b) total liquid content between the upper an lower portions of the boundary layer. The Buoyancy Integral Ratio (BIR, Bretherton and Wyant 1997) plotted in (c) is a measure of decoupling, with the plotted gray line at BIR = 0.15 indicating the decoupling threshold of Bretherton and Wyant.

	Minimum	Maximum	Mean	Median	75th	25th	N
LWF (W m^{-2})	0.00	110.45	84.59	89.27	95.60	77.10	207
LWF_0 (W m^{-2})	0.00	67.61	39.20	40.59	49.11	32.49	207
cf	0	1	0.86	1	1	1	207
ΔF_n (W m^{-2})	0.00	109.36	78.01	85.45	93.86	65.90	207
Z_{ct} (km)	0.78	1.84	1.3	1.29	1.42	1.17	186
LWF* (W m^{-2})	38.39	109.36	84.41	89.19	95.10	76.80	179
ΔF_n* (W m^{-2})	38.39	109.36	83.78	88.29	95.10	75.30	179
Z_{ct}* (km)	0.775	1.837	1.309	1.291	1.429	1.190	179

Table 1. Statistics calculated from the VOCALS ship soundings and the radiative flux calculations. Minimum, maximum, mean, median, and 75th and 25th percentile values are tabulated along with the number of soundings (N) analyzed for each metric. *LWF* refers to the radiative forcing calculated from the LWC profile whereas LWF_0 is the radiative forcing from the same thermodynamic profiles but assuming cloud-free conditions (i.e., the LWC profile set to zero). *cf* refers to cloud fraction. The net flux (ΔF_n) is the calculated by weighting *LWF* and LWF_0 by *cf*. Z_{ct} is the cloud-top height of the soundings. ΔF_n* and Z_{ct}* are conditionally sampled properties from soundings in which $cf > 0.5$ and $\Delta F_n > 0$.

References

Ackerman, A. S., and Coauthors, 2009: Large-eddy simulations of a drizzling, stratocumulus-topped marine boundary layer. *Mon. Wea. Rev.*, **137**, 1083–1110.

Albrecht, B. A., C. S. Bretherton, D. Johnson, W. H. Schubert, and A. S. Frisch, 1995a: The Atlantic stratocumulus transition experiment - ASTEX. *Bull. Am. Meteorol. Soc*., **76**, 889–904.

Bony, S. and J.-L. Dufresne, 2005: Marine boundary layer clouds at the heart of cloud feedback uncertainties in climate models. *Geophys. Res. Lett*., in press.

Bretherton, C. S. and M. C. Wyant, 1997: Moisture transport, lower-tropospheric stability, and decoupling of cloud-topped boundary layers. *J. Atmos. Sci*., **54**, 148–167.

Burleyson, C. D., 2013: Ship-Based Observations of the Diurnal Cycle of Southeast Pacific Marine Stratocumulus Clouds and Precipitation. *J. Atmos. Sci*., **70**, 3876–3892.

Burleyson, C.D., 2015: Subdiurnal Stratocumulus Cloud Fraction Variability and Sensitivity to Precipitation. *J. Climate*., 28, 2968-2985.

Deardorff, J. W., 1980a: Cloud top entrainment instability. *J. Atmos. Sci*., **37**, 561–563.

de Szoeke, S. P., Yuter, S. E., Mechem, D. B., Fairall, C. W., Burleyson, C. D., and Zuidema, P. 2012. Observations of Stratocumulus Clouds and Their Effect on the Eastern Pacific Surface Heat Budget along 20S. Journal of Climate, 25, 8542-8567.

Fu, Q. and K.-N. Liou, 1992. On the correlated k-distribution method for radiative transfer in nonhomogenous atmospheres. J. Atmos. Sci., 42, 2139-2156.

Fu, Q. and K.-N. Liou, 1993. Parameterization of the radiative properties of cirrus cloud. J. Atmos. Sci., 50, 2008-2025.

Hartmann, D. and D. Short, 1980: On the use of earth radiation budget statistics for studies of clouds and climate. *J. Atmos. Sci*., **37**, 1233–1250.

Jones, C. R., C. S. Bretherton, and D. Leon, 2011: Coupled vs. decoupled boundary layers in VOCALS-REx. *Atmos. Chem. Phys.*, **11**, 7143-7153.

Khairoutdinov, M. F., and D. A. Randall, 2003: Cloud resolving modeling of the ARM summer 1997 IOP: Model formulation, results, un-certainties, and sensitivities. *J. Atmos. Sci*., **60**, 607–625.

Kogan, Y. L., 1991: The simulation of a convective cloud in a 3-D model with explicit

microphysics. Part I: Model description and sensitivity experiments. *J. Atmos. Sci*., **48**, 1160–1189.

Krueger, S. K., G. T. McLean, and Q. Fu, 1995b: Numerical simulation of the stratus-to-cumulus transition in the subtropical marine boundary layer. Part II: Boundary layer circulation. *J. Atmos. Sci*., **52**, 2851–2868.

Lilly, D. K., 1968: Models of cloud-topped mixed layers under a strong inversion. Quart. *J. Roy. Meteorol*. Soc., **94**, 292–309.

Mechem, D. B. and Y. Kogan, 2003: Simulating the transition from drizzling marine stratocumulus to boundary layer cumulus with a mesoscale model. *Mon. Wea. Rev*., **131**, 2342–2360.

Mechem, D.B., Y. L. Kogan, and D. M. Shultz, 2010: Larg-Eddy Observation of Post-Cold-Frontal Continental Stratocumulus. *J. Atmos. Sci.*, **67**, 3368–3383.

Mechem, D. B., S. E. Yuter, and S. P. de Szoeke, 2012: Thermodynamic and aerosol controls in southeast Pacific stratocumulus. *J. Atmos. Sci.*, **69**, 1250–1266.

Mechem, D. B., S. E. Giangrande, C. S. Wittman, P. Borque, T. Toto, and P. Kollias, 2015: Insights from modeling and observational evaluation of a precipitating continental cumulus event observed during the MC3E field campaign. *J. Geophys. Res. Atmos.*, **120**, 1980–1995, doi:10.1002/2014JD022255.

Medeiros, B., B. Stevens, I. M. Held, M. Zhao, D. L. Williamson, J. G. Olson, and C. S. Bretherton, 2008: Aquaplanets, climate sensitivity, and low clouds. *J. Climate*, **21**, 4974–4991.

Medeiros, B., and B. Stevens, 2011: Revealing differences in GCM representations of low clouds. *Clim. Dyn*., **36**, 385–399

Nicholls, S., 1984: The dynamics of stratocumulus: aircraft observations and comparisons with a mixed layer model. *Quart. J. Roy. Meteorol. Soc*., **110**, 783–820.

Nicholls, S., 1986: An observational study of the structure of stratiform cloud shhets: Part I. Structure. *Quart. J. Roy. Meteorol. Soc*., **112**, 431-460

Park, S., C. Deser, and M. Alexander, 2005: Estimation of the surface heat flux response to sea surface temperature anomalies over the global oceans. *J. Climate*, **18**, 4582–4599.

Savic-Jovcic, V. and B. Stevens, 2008: The structure and mesoscale organization of precipitating stratocumulus. *J. Atmos. Sci*., **65**, 1587–1605.

Schubert, W. H., J. S. Wakefield, E. J. Steiner, and S. K. Cox, 1979a: Marine stratocumulus convection. Part I: Governing equations and horizontally homogeneous solutions. *J. Atmos. Sci*., **36**, 1286–1307.

Slingo, A., 1990: Sensitivity of the Earth's radiation bud- get to changes is low clouds. *Nature*, **343**, 49–51.

Snodgrass, E. R., L. Di Girolarmo, and R. M. Rauber, 2008. Precipitation Characteristics of Trade Wind Clouds during RICO Derived from Radar, Satellite, and Aircraft Measurements. *J. Atmos. Sci*., **48**, 464-483.

Stephens, G. L. and T. J. Greenwald, 1991: Observations of the Earth's radiation budget in relation to atmospheric hydrology. Part II: Cloud effects and cloud feedback. *J. Geophys. Res*, **96**, 15 325–15 340.

Stevens, B., W. R. Cotton, G. Feingold, and C.-H. Moeng, 1998: Large-eddy simulations of strongly precipitating, shallow, stratocumulus-topped boundary layers. *J. At- mos. Sci*., **55**, 3616–3638.

Stevens, B., G. Vali, K. Comstock, R. Wood, M. vanZanten, P. H. Austin, C. S. Bretherton, and D. H. Lenschow, 2005a: Pockets of open cells (POCs) and drizzle in marine stratocumulus. *Bull. Am. Meteor. Soc*., **86**, 51–5

Stevens, B., et al., 2005b: Evaluation of large-eddy simulations via observations of nocturnal marine stratocumulus. *Mon. Wea. Rev*., **133 (6)**, 1443–1462.

Stevens, B., and S. Bony, 2013: What are climate models missing? *Science*, **340**(6136), 1053-1054.

vanZanten, M. C. and B. Stevens, 2005: Observations of the structure of heavily precipitating marine stratocumulus. *J. Atmos. Sci*., **62**, 4327–4342.

Wang, H., and G. Feingold, 2009a: Modeling mesoscale cellular structures and drizzle in marine stratocumulus. Part I: Impact of drizzle on the formation and evolution of open cells. J. Atmos. Sci., 66, 3237–3256.

Wang, H., and G. Feingold, 2009b: Modeling mesoscale cellular structures and drizzle in marine stratocumulus. Part II: The microphysics and dynamics of the boundary region between open and closed cells. *J. Atmos. Sci.*, **66**, 3257–3275.

Warren, S. G., C. J. Hahn, J. London, R. M. Chervin, and R. L. Jenne, 1986: Global distribution of total cloud cover and cloud types over land. *NCAR Technical Note* NCAR/TN-273+STR 29pp+200 maps, National Center for Atmospheric Research, Boulder, CO.

Wood, R., T., 2012: Stratocumulus Clouds. University of Washington, Seattle, WA.

Wyant, M. C., C. S. Bretherton, H. A. Rand, and D. E. Stevens, 1997: Numerical simulations and a conceptual model of the stratocumulus to trade cumulus transition. *J. Atmos. Sci*., **54**, 168–192.

Young, C. S., Cameron, B.K. and E.E. Hebble, 2000. Observations of the Entrainment Zone in a Rapidly Entraining Boundary Layer. *J. Atmos. Sci*., **57**, 3145-3160.

Yuter, S. E., and R. A. Houze Jr., 1995: Three-dimensional kinematic and microphysical evolution of Florida cumulonimbus. Part II: Frequency distribution of vertical velocity, reflectivity, and differential reflectivity. *Mon. Wea. Rev.*, **123**, 1941–1963.

Zuidema, P., E. Westwater, C. Fairall and D. Hazen, 2005: Ship-based Liquid Water Path Estimates in Marine Stratocumulus. *J. Geophys. Res.*, **110**, D20206, doi:10.1029/2005JD005833.